Hematite (α-Fe_2O_3) with Various Morphologies: Ionic Liquid-Assisted Synthesis, Formation Mechanism, and Properties

Jiabiao Lian, Xiaochuan Duan, Jianmin Ma, Peng Peng, Tongil Kim, and Wenjun Zheng*

Department of Materials Chemistry, College of Chemistry, Nankai University, Tianjin, 300071 P. R. China

ABSTRACT The α-Fe_2O_3 with various morphologies has been successfully synthesized *via* an ionic liquid-assisted hydrothermal synthetic method. The samples are characterized by X-ray diffraction, Fourier transform infrared spectroscopy, field emission scanning electron microscope (FE-SEM), transmission electron microscopy, and high-resolution transmission electron microscopy. The results indicate that the as-prepared samples are α-Fe_2O_3 nanoparticles, mesoporous hollow microspheres, microcubes, and porous nanorods. The effects of the ionic liquid 1-*n*-butyl-3-methylimidazolium chloride ([bmim][Cl]) on the formation of the α-Fe_2O_3 with various morphologies have been investigated systematically. The proposed formation mechanisms have also been investigated on the basis of a series of FE-SEM studies of the products obtained at different durations. Because of the unique porous structure, the potential application in water treatment of the α-Fe_2O_3 porous nanorods was investigated. The UV—vis measurements suggest that the as-synthesized pure α-Fe_2O_3 with various morphologies possess different optical properties depending on the shape and size of the samples. The magnetic hysteresis measurements indicate the interesting magnetic property evolution in the as-prepared α-Fe_2O_3 samples, which is attributed to the superstructure or the shape anisotropy of the samples. This method is expected to be a useful technique for controlling the diverse shapes of crystalline inorganic materials for a variety of applications, such as sensors, gas and heavy metal ion adsorbents, catalytic fields, hydrogen and Li ion storage, and controlled drug delivery, *etc.*

KEYWORDS: hematite · ionic liquid · superstructures · porous materials · magnetic properties

The controlled fabrication of nanostructured materials with functional properties has attracted more and more attention in recent years for their unique size and shape-dependent properties (optical, electrical, magnetic, catalytic, mechanical, chemical, *etc.*).[1−3] Therefore, studies on the shape controllable synthesis of nanomaterials are of great interest and are actively being pursued. In particular, many efforts have been devoted to a precise control of hollow and porous structures with uniform sizes,[4−14] due to their low effective density, high specific surface area, and potential scale-dependent applications in catalysis, drug delivery, active material encapsulation, ionic intercalation, lightweight filler, surface functionalization, energy storage, and so on. Semiconductor nanomaterials have been identified as important materials with potential applications in a wide range of fields.[15,16] Hematite (α-Fe_2O_3), an n-type semiconductor (E_g = 2.1 eV), is the most thermodynamically stable phase of iron oxide. It has been extensively investigated in catalysts, pigments, gas sensors, magnetic recording media, optical devices, and electromagnetic devices, owing to its nontoxicity, low processing cost, and high resistance to corrosion. Many recent efforts have been directed toward the fabrication of nanostructural iron oxides to enhance their performance in currently existing applications. To date, well-defined nanostructures of iron oxides with different dimensionalities such as nanoparticles, nanorods, nanowires, nanotubes, nanorings, nanobelts, nanocubes, as well as hollow and porous nanostructures have been obtained successfully by a series of solution-based routes and vapor-phase processes.[17−30] As expected, these α-Fe_2O_3 nanostructures lead to interesting size and shape-dependent properties and a wide variety of potential applications,[31−39] including gas sensors, electrode materials in lithium secondary batteries, catalysts, magnetic recording media, and optical and electromagnetic devices as well as water splitting and pollution treatment. Among various synthesis methods, template-directed approaches including hard templates (*e.g.*, polymer latex, carbon, anodic aluminum oxide templates) or soft-templates (*e.g.*, supramolecular, surfactant, organogel) have been extensively investigated. For example, Zhong *et al.*[36] have reported the synthesis of flowerlike iron oxide nanostructures in the

*Address correspondence to zhwj@nankai.edu.cn.

Received for review August 5, 2009 and accepted October 27, 2009.

Published online October 30, 2009.
10.1021/nn900941e CCC: $40.75

presence of urea and tetrabutylammonium bromide (TBAB) by a solvothermal process with subsequent calcination. Zeng *et al.*[39] have synthesized hollow hematite spindles and microspheres using $FeCl_3$, oxalic acid, and bases as reactants at first, and then calcined the precursors in air at 400 °C for 2 h. These synthesis routes seem to be inconvenient because complete template removal is needed, which means a much more complicated process including the selection of appropriate solvent or calcination at elevated temperature. Furthermore, the removal of the surfactants or shape-control ions will always bring a negative effect on the morphology of the products. In addition, the previous synthetic routes are often time-consuming and need precursor calcination steps. Therefore, it still remains a challenge to develop a facile and environmental friendly route to synthesize the morphology controllable hematite.

Room-temperature ionic liquids (RTILs), as green and efficient recyclable solvents, have gained a great deal of both academic and industrial attention as a new class of compounds for a potential effective green replacement of conventional organic solvents for long-lasting development of human society.[40−42] Because of their highly favorable properties, such as extremely low volatility, good thermal stability, good dissolving ability, wide liquid temperature range, designable structures, high ionic conductivity, and wide electrochemical window, RTILs have been used effectively in organic chemical reactions, separation, and electrochemical processes.[43−46] The most important advantage of ILs, however, is that ILs can form extended hydrogen bond systems in the liquid state and are therefore highly structured.[47] This special quality can be used as the "entropic driver" for spontaneous, well-defined, and extended ordering of nanoscale structures. More recently, the synthesis of nano- and microstructured inorganic materials in ILs has aroused increasing attention because of their excellent properties. It has been demonstrated that ILs not only can be used as functional solvents but also as templates for the preparation and stabilization of various inorganic nanomaterials with novel and improved properties.[48−52] For instance, in the previous work, our group has successfully synthesized pure rutile and rutile-anatase composite TiO_2 nanoparticles *via* an ionic liquid-assisted method,[53] and has also prepared a series of shape-controllable ZnO nanocrystals stabilized by different ionic liquids,[54] which show tunable photoluminescence and high photocatalytic activity. S. W. Cao *et al.*[52] have recently fabricated hematite nanostructures *via* the microwave-hydrothermal ionic liquid method. However, it also needed the transformation from FeOOH crystallites to hematite by calcination at high temperature, and the authors have not investigated the effects of the ionic liquid [bmim][BF_4] in detail. In contrast to their application in organic chemistry, the use of RTILs in inorganic synthesis is still in its primary stage, and more exploration is necessary to utilize their advantages fully.

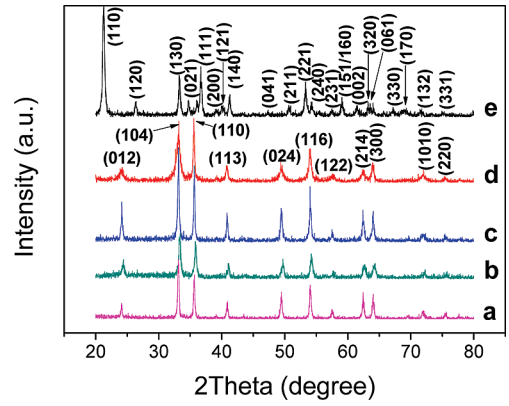

Figure 1. XRD patterns of as-synthesized samples: (a) S-1, α-Fe_2O_3 nanoparticles; (b) S-2, α-Fe_2O_3 mesoporous hollow microspheres; (c) S-4, α-Fe_2O_3 microcubes; (d) S-5, α-Fe_2O_3 nanorods; (e) α-FeOOH nanorods (S-5 before annealing).

Herein, we report a novel and environmentally benign green route to synthesize the α-Fe_2O_3 with various morphologies *via* an ionic liquid-assisted hydrothermal synthetic method. Some fascinating features are described in the present work. (i) This method is very simple. The synthesis of the α-Fe_2O_3 nanoparticles, mesoporous hollow microspheres, and microcubes is a one-step process that does not require high temperature or high pressure. (ii) The ionic liquid [bmim][Cl], a green recyclable solvent, plays a strategic role on the shape of the α-Fe_2O_3 as a soft template or a capping agent, which can be easily and effectively removed. The effects of the [bmim][Cl] have been investigated systematically. (iii) The UV−vis and magnetic hysteresis measurements suggest that the as-synthesized pure α-Fe_2O_3 with various morphologies possess different optical and magnetic properties depending on the shape and size of the samples, respectively. Due to the unique porous structure, the potential application in water treatment of the α-Fe_2O_3 porous nanorods was investigated. As far as our knowledge, it is the first time that one-step ionic liquid-assisted hydrothermal synthesis of the α-Fe_2O_3 mesoporous hollow microspheres and microcubes assembled by nanoparticles has been reported. The proposed formation mechanisms of the α-Fe_2O_3 with various morphologies have also been investigated.

RESULTS AND DISCUSSION

Structure Characterization. The purity and crystallinity of as-prepared samples were examined using powder XRD measurements (Figure 1). Figure 1a−d are the XRD patterns of the as-prepared α-Fe_2O_3 nanoparticles (S-1), mesopoprous hollow microspheres (S-2), microcubes (S-4), and nanorods (S-5, obtained by annealing the as-prepared α-FeOOH nanorods in air at 250 °C for 3 h), respectively. It is evident that all of the expected peaks can be indexed to the hexagonal structure of

α-Fe_2O_3 (space group: $R\bar{3}c$, No. 167) with structural parameters of $a = b = 5.038$ Å, $c = 13.772$ Å, $\alpha = \beta = 90°$, and $\gamma = 120°$, which are in good agreement with the literature results (*i.e.*, JCPDS Card 33-0664). The narrow sharp peaks suggest that the α-Fe_2O_3 products are highly crystalline. No other peaks are observed, indicating the high purity of the as-prepared samples. Figure 1e is the XRD pattern of the as-obtained α-FeOOH nanorods, where all the diffraction peaks can be indexed as orthorhombic α-FeOOH (space group: *Pbnm*, No. 62) with cell constants of $a = 4.608$ Å, $b = 9.956$ Å, and $c = 3.022$ Å, which is consistent with the reported data (JCPDS Card 29-0713). Further evidence for the formation of the α-FeOOH can be obtained from the FT-IR spectrum of the sample, as shown in Figure S1a (see the Supporting Information). The strong peaks at 3120, 892, 791, and 628 cm^{-1} are the characteristic vibrations in the α-FeOOH product.[55] These peaks disappeared and two new strong absorption peaks observed after calcination at 250 °C for 3 h, as shown in Supporting Information, Figure S1b, which shows the peaks at 545 and 470 cm^{-1} assigned to Fe-O characteristic vibrations of α-Fe_2O_3,[56] indicating the formation of the α-Fe_2O_3 phase.

According to the full width at half-maximum (fwhm) of the diffraction peaks, the average crystallite size of the as-prepared nanoparticles and hollow microspheres can be estimated from the Scherrer equation to be about 39.1 and 35.3 nm, respectively.

$$D_{hkl} = K\lambda/(\beta_{hkl} \cos \theta_{hkl})$$

where D_{hkl} is the particle size perpendicular to the normal line of (*hkl*) plane, K is a constant (it is 0.9), β_{hkl} is the full width at half-maximum of the (*hkl*) diffraction peak, θ_{hkl} is the Bragg angle of (*hkl*) peak, and λ is the wavelength of X-ray.

Morphology Characterization. The field emission scanning electron microscopy (FE-SEM) and corresponding transmission electron microscopy (TEM) images of the S-0 obtained without the [bmim][Cl] are shown in the Figure S2 (see the Supporting Information). It can be seen that the morphology and the size are not uniform and the particles reunite badly. Supporting Information, Figure S2c is the XRD pattern of the S-0, which indicates the sample has pure hematite phase. Detailed morphology studies of the samples obtained with the [bmim][Cl] in the CH_3COOK system have been carried out in Figure 2. Figure 2a shows the FE-SEM image of the S-1, which is composed of uniform monodispersed nanoparticles. A higher magnification FE-SEM image shown in Figure 2b indicates that the surfaces of these nanoparticles with an average size of 40 nm are relatively rough, which is further confirmed by the corresponding low-magnification and high-magnification TEM images, as shown in Figure 2c and the up-right inset, respectively. The typical lattice fringe spacing shown in the high-resolution TEM (HRTEM) image (Figure 2d) is determined to be 0.252 nm, corresponding to the (110) lattice plane of α-Fe_2O_3.

Figure 2e is the low-magnification FE-SEM image of the S-2, which shows a spherical morphology with an average diameter of about 1 μm. Although the average diameter of α-Fe_2O_3 microspheres (secondary particles) is far larger than the particle size based on X-ray diffraction (XRD) analysis, the high-magnification FE-SEM and TEM images (Figure 2 panels f and h, respectively) give the evidence that the microspheres are composed of individual nanoparticles (primary particles) with an average size of about 40 nm, which is consistent with the result calculated from Scherrer's formula. To reveal the hollow nature of the α-Fe_2O_3 microspheres, the microspheres were broken by ultrasonic treatment. As shown in the inset of Figure 2e, one α-Fe_2O_3 microsphere is broken, which clearly shows the hollow nature of the α-Fe_2O_3 microspheres. The corresponding TEM image of the microspheres as shown in Figure 2g further confirms the hollow microsphere structure with a shell thickness of about 200 nm around. It also can be seen that there are some pale areas between the dark nanoparticles, which indicates the existence of mesoporous nanostructures on the shell of the hollow microspheres. The higher magnification TEM (Figure 2h) further clearly identifies the mesoporous nanostructures on the shell of the hollow microspheres and reveals that the size of the mesoporosity is about 10−50 nm. Figure 2 panels I and j are the FE-SEM images of the similar mesoporous hollow microspheres with a larger diameter (about 2 μm) obtained in the higher concentration [bmim][Cl] (S-3). The HRTEM image of the α-Fe_2O_3 mesoporous hollow microspheres (Figure 2k) is the same as that of the microcubes (Figure 3e), which shows the lattice image obtained at the edge of the particle. The typical lattice fringe spacings are determined to be 0.370 and 0.210 nm, corresponding to the (012) and (202) *d* spacing of the hexagonal α-Fe_2O_3, respectively, which clearly demonstrate that the mesoporous hollow microspheres and microcubes consist of the single crystalline nanoparticles. The hexagonal-like spot arrays (Figure 3f) shown by the fast Fourier transform spectrum (FFT) further verifies the single-crystal nature of the nanoparticles and hexagonal crystal structure of the α-Fe_2O_3.

The morphology of the α-Fe_2O_3 microcubes with highly geometrical symmetry was visualized by FE-SEM and TEM. Typical low-magnification FE-SEM image of Figure 3a clearly shows the product possesses a large-scale uniform cubic structure. The high-magnification FE-SEM (Figure 3b) and corresponding TEM (Figure 3c) images display that the size of the cubes is about 600 nm in edge and the surfaces of the microcubes are relatively rough, which is further confirmed by the high-magnification TEM (Figure 3d). The HRTEM image of

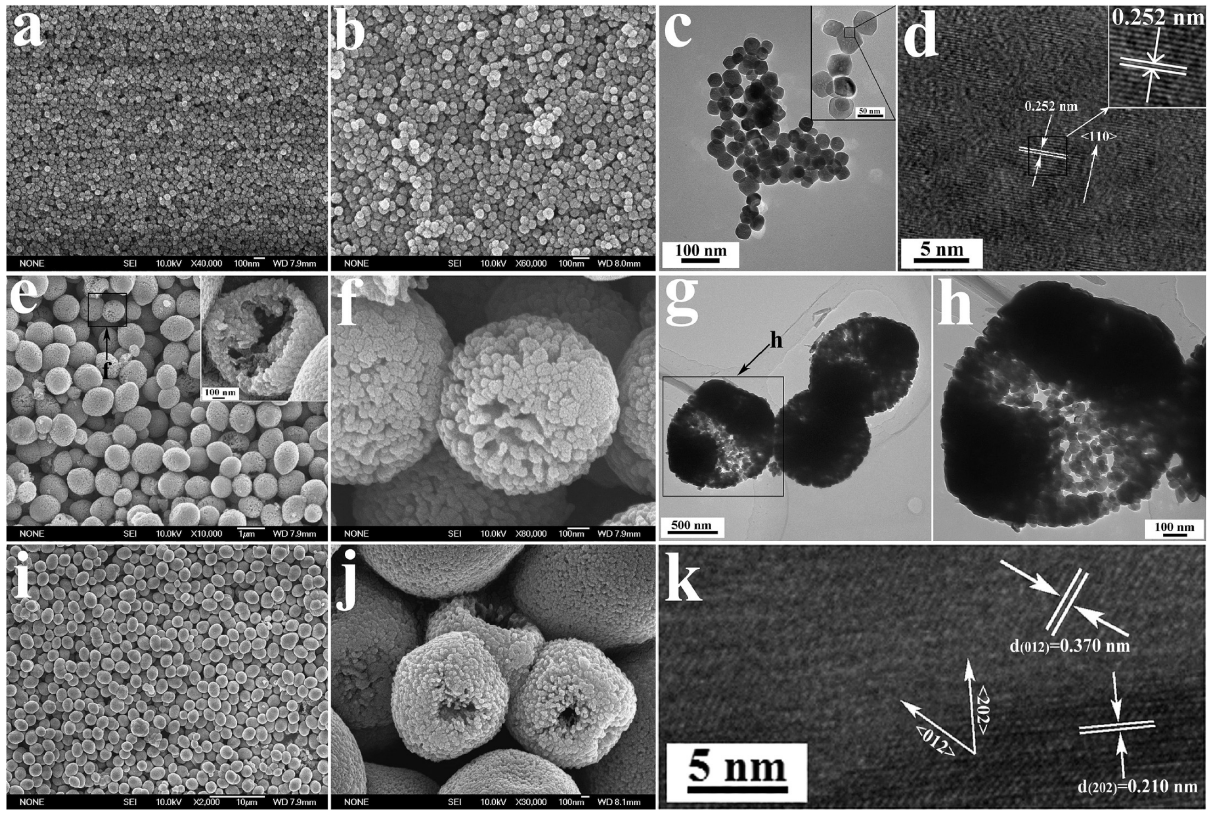

Figure 2. FE-SEM, TEM, and HRTEM images of the samples obtained in CH_3COOK system at 150 °C for 8 h: (a) low-magnification and (b) high-magnification FE-SEM, (c) Corresponding low-magnification and high-magnification (the inset) TEM and (d) HRTEM images of α-Fe_2O_3 nanoparticles (S-1); FE-SEM (e, f) and TEM (g, h) images of α-Fe_2O_3 hollow microspheres with mesoporous shell (S-2), the inset in panel e clearly shows the hollow microsphere structure of S-2; (i) low-magnification and (j) high-magnification FE-SEM images of the larger α-Fe_2O_3 mesoporous hollow microspheres (S-3); (k) HRTEM image of the mesoporous hollow microsphere (S-2).

Figure 3e was taken from the area labeled e in Figure 3d.

Figure 4a represents the typical SEM image of the α-FeOOH nanorods, where rodlike morphology can be seen with a diameter in the nanometer range and length in submicrometers. The sample was characterized further by TEM to obtain more information on the structure and morphology. The typical TEM image in Figure 4b shows the nanorods having diameters in the range of 30−80 nm and length of 400−800 nm. A HRTEM image of the tip portion of a nanorod showing the clear fringes is displayed in Figure 4c. The interlayer spacings of 0.258, 0.249, and 0.151 nm correspond to the (021)/(0$\bar{2}$1), (040), and (002) plane of the α-FeOOH, respectively. This suggests that the growth occurs along the tip of the nanorod, that is, toward the [002] direction. The clear constant lattice fringes indicate that each nanorod is single crystalline nature. On the basis of the HRTEM result presented above, a structure model of the α-FeOOH nanorods is put forward in Figure 4d, which extends along [002] and is enclosed by the top/bottom surfaces (021)/(0$\bar{2}$1) and the side surface (040). Figure 4e−g shows the morphology of α-Fe_2O_3 porous nanorods obtained by heating the as-prepared α-FeOOH precursor. It is worth noting that the morphology was successfully maintained after thermal transformation of the precursor to α-Fe_2O_3, except that a lot of pores which were open to the outer surface and almost isolated from each other appeared within the annealed α-Fe_2O_3 nano-

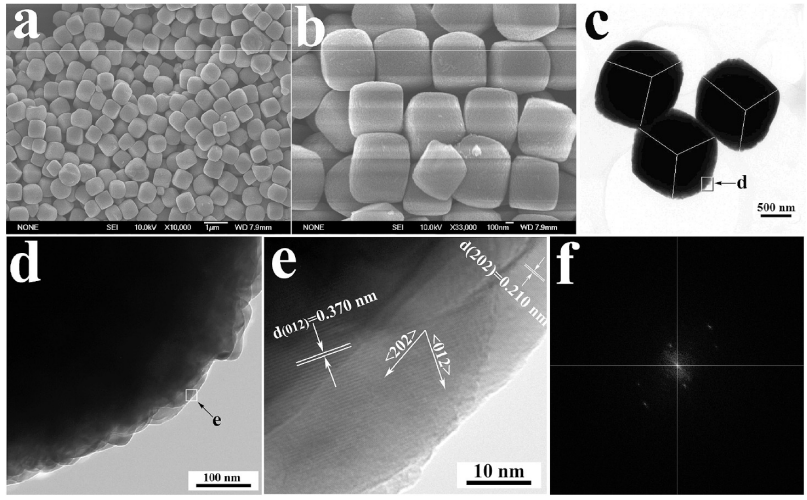

Figure 3. (a) Low-magnification and (b) high-magnification FE-SEM, (c, d) corresponding TEM, and (e) HRTEM images of α-Fe_2O_3 microcubes (S-4) obtained in NaOH system at 150 °C for 8 h. (f) The corresponding FFT of the HRTEM image.

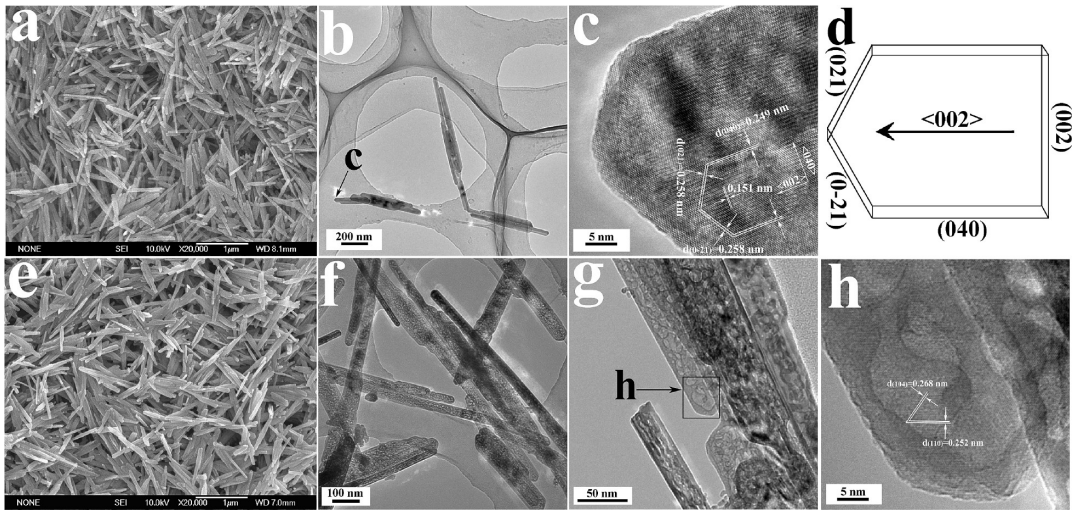

Figure 4. (a) FE-SEM, (b) corresponding TEM, and (c) HRTEM images of α-FeOOH nanorods obtained in NaOH system at 150 °C for 8 h; (d) a structural model of the α-FeOOH nanorod; (e) FE-SEM, (f, g) corresponding TEM, and (h) HRTEM images of α-Fe_2O_3 porous nanorods (S-5) obtained by heating the α-FeOOH nanorods.

rods. The size of the pores is in the range of 2−5 nm, which can be seen more clearly in higher magnification images in Figure 4g,h, and is further confirmed by Brunauer−Emmett−Teller (BET) surface area measurement and the pore size distribution analysis (Figure 5a). This porous network is believed to favor the adsorption of the organic pollutant in water treatment. The lattice fringe spacings in the HRTEM image (Figure 4h) taken from the area labeled h in Figure 4g are determined to be 0.252 and 0.268 nm, corresponding to the (110) and (104) *d* spacing of the hexagonal α-Fe_2O_3, respectively, which clearly demonstrate the single crystalline nature of the α-Fe_2O_3 porous nanorods.

Effect of the [bmim][Cl] on the Formation of the α-Fe_2O_3 with Various Morphologies. To investigate the effect of the ionic liquid [bmim][Cl] on the formation of hematite with various morphologies, a series of comparative experiments (as shown in Table 1) were carried out.

On the basis of the results above, it can be indicated that the ionic liquid [bmim][Cl] plays a crucial role on the morphology of the α-Fe_2O_3. We consider that the possible reasons mainly involve some aspects. First, it is well-known that the size of the products depends on the rate of nucleation and the growth rate of the product. Although the ionic liquids show polar features, they have low surface tensions compared with water. Lower interface tension results in a high nucleation rate, which is faster than the growth rate. Consequently, very small particles (S-1) can easily be generated.[57,58] Moreover, the presence of a small amount of [bmim][Cl] can effectively control the reunion of the nanoparticles and well improve the dispersion in the reaction system just as the simple surfactant. Second, when the amount of

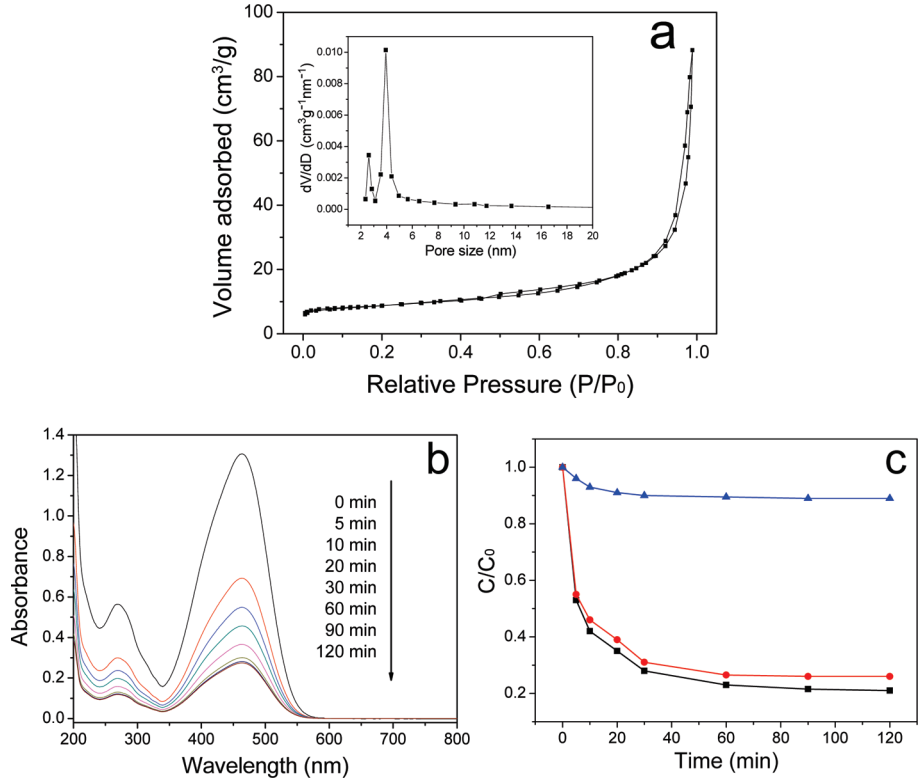

Figure 5. (a) Nitrogen adsorption-desorption isothermal and the pore size distribution curve (inset) for the α-Fe_2O_3 porous nanorods; (b) UV−vis absorption spectra of MO solutions after treated with α-Fe_2O_3 porous nanorods at different time intervals; (c) Adsorption rate of MO on new as-prepared (black line) and regenerated (red line) α-Fe_2O_3 porous nanorods, and commercial α-Fe_2O_3 (blue line).

TABLE 1. Experimental Conditions for the Preparation of Samples

reaction system		sample number	[bmim]Cl (mol/L)	morphology	size (nm)
CH_3COOK system	1:3[a]	S-0	0	irregular nanoparticles	40−300
	1:3[a]	S-1	0.05	nanoparticles	40
	1:3[a]	S-2	0.3	mesoporous hollow microspheres	1000
	1:3[a]	S-3	0.5	mesoporous hollow microspheres	2000
NaOH system	1:3[b]	S-4	0.3	microcubes	600
	1:10[b]	S-5	0.3	porous nanorods	30−80 (diameter) 400−800 (length)

[a]The mole ratio of $FeCl_3 \cdot 6H_2O/CH_3COOK$; [b]The mole ratio of $FeCl_3 \cdot 6H_2O/NaOH$.

the [bmim][Cl] increased, the morphology of the hematite changed from monodispersed nanoparticles to the superstructures (mesoporous hollow microspheres and microcubes). As we know, a typical Ostwald ripening process involving the formation of larger crystals by greatly reducing the interfacial energy of small primary nanocrystals is energetically favored. However, the interactions between unprotected building units with nanoscale size are generally not competent to form stable and uniform microstructures,[59−61] such as the mesoporous hollow microspheres and microcubes discussed here. Moreover, the building blocks would always randomly aggregate into disordered crystals rather than single crystals in the absence of sufficiently strong surface-protecting layers.[62] Therefore, in the work reported here, the presence of the [bmim][Cl] was believed to play a strategic role on the formation of this unique self-assembled superstructures as a soft template and a capping agent, which is due to the important advantage of ILs that can form extended hydrogen bond systems in the liquid state and are therefore highly structured. We[53,63] and others[64−68] have demonstrated the synthesis of nanostructures by ionic liquid assisted route, and the hydrogen bond-*co*-π−π stack mechanism is helpful to understand the influence of ionic liquids on the morphologies control of nanostructures. In the present case, the formation of the α-Fe_2O_3 superstructures can be possibly explained by the hydrogen bond-*co*-π−π stack mechanism. According to our previous work,[53,54] the cations of ionic liquid can be easily adsorbed on the surface of the O^{2-}-terminated surface by electrostatic force, and the hydrogen bond, formed between the hydrogen atom at C2 position of the imidazole ring and the oxygen atoms of O−Fe, may act as an effective bridge to connect the O^{2-}-terminated plane of the produced nuclei of metal oxide and cations of ionic liquids. The $[bmim]^+$ cations will be aligned to facilitate the proposed relocation of the molecules based on its ability to self-assemble into ordered structures stabilized by additional π−π interactions between the imidazolium rings of [bmim][Cl], thus resulting in the self-organization of the nanoparticles into the desired superstructures.

To confirm the discussions above, FTIR spectra of pure [bmim][Cl] and α-Fe_2O_3/[bmim][Cl] are performed in Figure S3 (as shown in Supporting Information), and the main frequencies of peaks are listed in Table S1 (as shown in Supporting Information). Compared with that of the pure [bmim][Cl], the FTIR spectrum of α-Fe_2O_3/[bmim][Cl] displays significant differences (the details are described in Supporting Information), which indicates the existence of the strong hydrogen bonds between the C2([bmim][Cl])-H-O(α-Fe_2O_3) and π−π stacking interaction of the imidazolium rings of [bmim][Cl].

In addition, as mentioned above, the diameter of the mesoporous hollow microspheres increased from 1 to 2 μm with increasing the amount of the [bmim][Cl]. We think it may be due to the viscosity of the medium.[69,70] Other groups[71,72] have demonstrated the viscosity of ionic liquids−water mixtures, which can generally be described by the exponential expression:

$$\eta = \eta_{IL} \exp(-x_C/a)$$

where x_C is the mole fraction of water, a is a characteristic constant of the mixture, and η_{IL} is the viscosity of the pure ionic liquid. The empirical equation above indicated that the viscosity of ionic liquids−water mixtures increased exponentially when the mole fraction of water (x_C) decreased. The increasing of the [bmim][Cl] amount increased the viscosity of the system, which hindered the diffusion of monomers. The influence of viscosity on the Ostwald ripening of α-Fe_2O_3 may be significant thereby, and the growth of nanocrystals for a diffusion-limited growth model, that is, the new hematite nuclei, preferred to aggregate on the surface of the already existed microspheres, rather than forming a new sphere. Put simply: the hindering diffusion effect of the [bmim][Cl] combined with the localized Ostwald ripening process is critical for the increase of the size of the mesoporous hollow microspheres.

Possible Formation Mechanism. To disclose the formation mechanism of α-Fe_2O_3 nanoparticles and mesoporous hollow microspheres, we performed several experiments that involved intercepting the intermediates at different reaction times to investigate the morphological evolution process of nanoparticles (Figure S4 in Supporting Information) and mesoporous hollow microspheres (Figure S5 in Supporting Information), respectively.

As shown in Figure S4a, the thin flakes were obtained after the hydrothermal treatment for 0.5 h. To minimize the overall energy of the system, these thin flakes grew into small seed particles, some of which had a tendency to aggregate together into micropolyhedrons (Figure S4b,c). When the reaction time prolonged to 4 h, the product was mainly composed of inhomogeneous nanoparticles with the diameter in the range of 100−150 nm. As reaction time reached to 6 h, well-defined and uniform nanoparticles with 100 nm in di-

ameter were obtained. When it finally came to 8 h, the diameter of the nanoparticles became smaller, indicating the dissolution process occurred. Furthermore, the surfaces of the nanoparticles became rough, indicating that the etching process occurred. The discussions above indicated that the CH_3COOH formed in the reaction was responsible for the dissolution as well as etching process.

On the basis of the above experimental results, the possible reaction mechanism in the CH_3COOK system may be illustrated as followed:

$$CH_3COO^- + H_2O \leftrightarrow CH_3COOH + OH^- \quad (1)$$

$$Fe^{3+} + 3OH^- \rightarrow Fe(OH)_3/FeOOH \xrightarrow{\text{hydrothermal condition}} \alpha\text{-}Fe_2O_3 \quad (2)$$

$$\alpha\text{-}Fe_2O_3 + 6CH_3COOH \leftrightarrow 2Fe^{3+} + 6CH_3COO^- + 3H_2O \quad (3)$$

As shown above, Fe^{3+} reacted with the OH^- produced by the hydrolysis of CH_3COO^- to form the yellow FeOOH suspension. The formation of solid-phase FeOOH (Supporting Information, Figure S5b) in reaction 2 was confirmed by XRD measurement (Figure S5g) during the hydrothermal treatment process. In addition, the yellow FeOOH powders were easily dehydrated during further hydrothermal treatment, consequently, the α-Fe_2O_3 nanoparticles could be obtained, as shown in Figure S5c. The corresponding XRD pattern (Figure S5g) indicated that these nanoparticles were pure α-Fe_2O_3 (JCPDS Card 33-0664). In the presence of [bmim][Cl], these nanoparticles had a tendency to self-assembled into microspheres (Figure S5d). However, these aggregated Fe_2O_3 microspheres are not in thermodynamically equilibrium status and become metastable because of their large surface energy. To reduce the total surface energy, the formed metastable α-Fe_2O_3 microspheres would remain out of equilibrium with the surrounding solution because of their higher solubility, so the core dissolves in the presence of CH_3COOH generated from the reaction (as shown in the eq 3), and the existence of a diffusion pathway through the outer crystalline shell results in the mesoporous structure (Figure S5e). The presence of relatively abundant CH_3COOH prompts the equation toward the right-hand side and enhances the degree of dissolution, which is similar to the previous results for the formation of α-Fe_2O_3 nanocrystals.[24,30,35] As a consequence, the supersaturation increases in the solution and then will be over the solubility of the crystalline Fe_2O_3; secondary nucleation of Fe_2O_3 occurs on the external surface. Thus, the thickness of the crystalline shell increases as the amorphous core becomes progressively depleted to produce intact hollow microspheres (Figure S5f). In summary, the growth process of the α-Fe_2O_3 mesoporous hollow microspheres undergoes three different stages. The nucleation and aggregation dominate at the initial stage. At the subsequent stage, self-assembly and dissolution−recrystallization process dominates, in which the dissolution-diffusion process (the effect of CH_3COOH) offers the opportunity to create the porosity on the shell and is of critical importance for the formation of the hollow structures. At the last stage an Ostwald ripening process dominates. The [bmim][Cl] mainly plays its role in the subsequent by the hydrogen bonds adsorption on the surface of the nanoparticles and make them self-assemble into microspheres. Moreover, the [bmim][Cl] can protect the exteriors of the microspheres, so the dissolution process preferentially occurs from the interiors of the microspheres. The α-Fe_2O_3 hollow microspheres with mesoporous shell have been successfully synthesized, due to the synergic effect of the CH_3COOH and [bmim][Cl], which comprises a dissolution effect and self-assembled as well as protective effect, respectively. On the basis of the discussions above, the growth process of the α-Fe_2O_3 mesoporous hollow microspheres can be illustrated in Scheme 1.

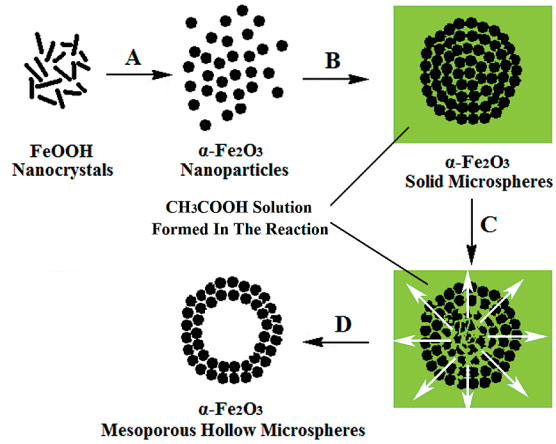

A: Hydrothermal Condition; B: Self-assembly in the presence of [bmim]Cl; C: Dissolution-Diffusion in the presence of CH_3COOH; D: Ostwald Ripening

Scheme 1. Schematic illustration for the growth process of the α-Fe_2O_3 mesoporous hollow microspheres.

In the CH_3COOK system, with the hydrolysis of Fe^{3+}, there are more and more CH_3COOH generated to form an acidic solution, in which the hematite nuclei are easily attacked by the protons. In contrast, the pH value of the NaOH system is decreasing with the reaction time increasing, and the solution even becomes close to neutral when the Fe^{3+} completely reacted with the OH^- (the mole ratio of $FeCl_3$ to NaOH is 1:3), which does not favor the dissolution of the hematite nuclei. Consequently, the nanoparticles self-assemble into the solid α-Fe_2O_3 microcubes in the presence of [bmim][Cl] in the NaOH system.

According to the literature,[73−75] the value of pH is determinant for the obtaining of goethite or hematite either through a dissolution−crystallization process or

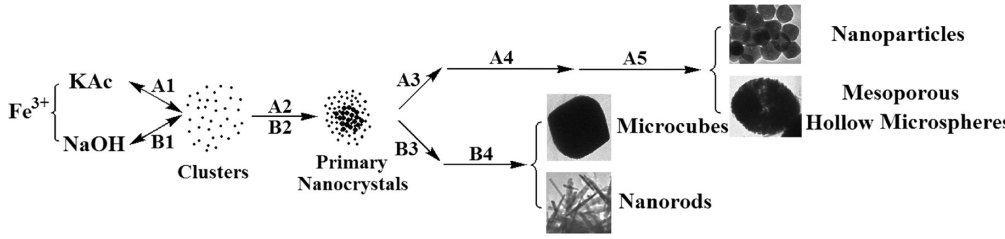

A1—A2—A3—A4—A5 : Nucleation—Aggregation—Dissolution—Recrystallization—Ostwald Ripening

B1—B2—B3—B4 : Nucleation—Aggregation—Recrystallization—Ostwald Ripening

Scheme 2. Schematic illustration for the formation mechanism of α-Fe_2O_3 crystals with various morphologies in different reaction systems.

through a solid-state transformation, and the present high value of pH (~14) favors the formation of goethite α-FeOOH. To understand the growth mechanism of the α-FeOOH nanorods, the products obtained at different reaction durations have also been analyzed through FE-SEM images (Figure S6) and the details were described in the Supporting Information. The α-Fe_2O_3 porous nanorods were obtained by heating the as-prepared α-FeOOH nanorods at 250 °C for 3 h, preserving the same rodlike morphology. This is not surprising because the crystal structures of α-FeOOH and α-Fe_2O_3 share a great commonality. It is well-known that α-FeOOH transforms to α-Fe_2O_3 with no great structural modifications but *via* a topotactic transformation.[75] The gentle structural modification allows α-Fe_2O_3 to retain the morphology, which is, in the present case nanorods. A lot of pores have been observed in the annealed α-Fe_2O_3 nanorods, due to the decomposition of the α-FeOOH and release of H_2O.

On the basis of the discussions above, two types of formation mechanisms[30] may be proposed for the growth of α-Fe_2O_3 with various morphologies in the presence of the [bmim][Cl]. One is "nucleation−aggregation−dissolution−recrystallization−Ostwald ripening" for the CH_3COOK system, and the other is "nucleation−aggregation−recrystallization−Ostwald ripening" for the NaOH system, as schematically depicted in Scheme 2.

Application in Waste Water Treatment. In recent years, considerable attention has been paid to the environmental problems involving water treatment. Compared with the traditional methods, the development of nanoscience and nanotechnology offers an alternative by using nanosorbents, nanocatalysts, and so on for the amelioration of current water treatment problems. Many researchers have used iron oxide hollow spindles and microspheres to remove toxic ions and organic pollutants from water, and these materials show higher removal capacities than bulk material.[76,77] However, there was little report on the porous nanorods used in the application of water treatment. Figure 5a shows the nitrogen adsorption−desorption isothermal and the pore size distribution curve (inset) for the α-Fe_2O_3 porous nanorods. The BET surface area of the as-obtained nanorods was 30.27 m^2/g. The BJH analyses showed that the α-Fe_2O_3 porous nanorods possessed bimodal mesopore distribution. The inset of Figure 5a displayed the main pore size distribution of 2.6 and 4.0 nm in the as-obtained nanorods. Because of its porous structure, we expect the as-obtained nanorods to be useful in the water treatments. As the size of the hematite nanorods was not too small, the solid/liquid separation would be easily separated by a facile method such as centrifugation. Herein, we used the as-prepared porous nanorods (S-5) to investigate its application in water treatment. Methyl orange (MO) was selected as the model organic pollutant. The initial concentration of the MO solution was set to be 20 mg/L.

UV−vis absorption spectroscopy was used to record the adsorption behavior of the solution after treatment. Figure 5b shows the evolution of MO absorption spectra in the presence of 40 mg α-Fe_2O_3 porous nanorods. The characteristic light absorption of MO at 463 nm was chosen to monitor the process of adsorption. As shown in Figure 5c, the whole adsorption process can be divided into two stages. In the first stage, MO was immediately adsorbed within 10 min ($C/C_0 = 0.42$), and in the following second stage from 10 to 120 min, MO molecules were adsorbed steadily ($C/C_0 = 0.21$). The removal capacity of the porous nanorods was calculated to be 39.5 mg/g. The favorable performance could be attributed to the highly porous structure and high surface area of the as-prepared sample. The removal of MO may be associated with the electrostatic attraction between the iron oxide surface and the MO molecules. Furthermore, the iron oxide containing MO could be regenerated by simply catalytic combustion at 400 °C in air for 2 h, and the regenerated α-Fe_2O_3 material kept almost the same adsorption performance as shown by the red line in Figure 5c. For a comparison, commercial α-Fe_2O_3 was also used to remove MO in wastewater. As shown by the blue line in Figure 5c, the commercial α-Fe_2O_3 showed much lower efficiency in removing MO from wastewater. The saturation adsorption capacity was 5.5 mg/g, mainly due to its low surface area. From the above discussion, due to the porous structure and the facile way of regeneration, the as-prepared α-Fe_2O_3 porous nanorods would be a highly promising candi-

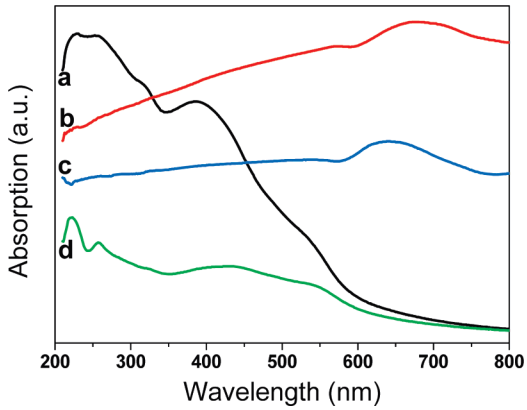

Figure 6. The size and shape-dependent UV−vis spectra of as-prepared α-Fe_2O_3 samples: (a) S-1, nanoparticles; (b) S-2, mesoporous hollow microspheres; (c) S-4, microcubes; (d) S-5, porous nanorods.

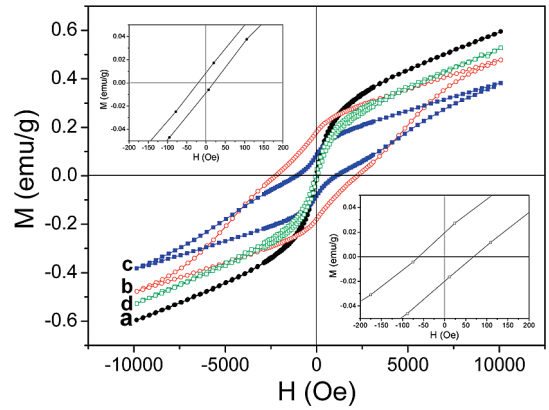

Figure 7. Magnetic hysteresis loops of as-prepared α-Fe_2O_3 samples at 300 K: (a) S-1, nanoparticles; up-left inset is a magnified view of curve a; (b) S-2, mesoporous hollow microspheres; (c) S-4, microcubes; (d) S-5, porous nanorods; down-right inset is a magnified view of curve d.

date to be applied in the water treatment for the environmental protection.

Optical Properties. Hematite nanomaterials have been used widely as ultraviolet absorbants for their broad adsorption in ultraviolet region from the electron transmission of Fe−O.[78] Herein, the optical absorption properties of the as-prepared α-Fe_2O_3 samples were investigated at room temperature by the UV−vis spectra (Figure 6). Such absorption is related to the shape and size of the samples. For instance, in the present case of the α-Fe_2O_3 nanoparticles (Figure 6a), the UV−vis band is mainly located in the far-UV region, with one intense broadband from 228 to 260 nm and a peak around 386 nm, which was consistent with the reported hematite nanoparticles.[79] Differing from the nanoparticles, the as-prepared mesoporous hollow microspheres with a size of 1 μm in diameter (Figure 6b) have a broadband around 680 nm, and microcubes with a size of 600 nm in edge (Figure 6c) have an intense broadband around 639 nm. It is mainly because when the α-Fe_2O_3 nanoparticles aggregate to be microcubes or microspheres, the size becomes larger, and then the scattering of visible light superimposes on the absorption of as-prepared superstructures.[80] Figure 6d shows the optical absorption spectrum of the α-Fe_2O_3 porous nanorods, and the optical absorption features were observed at wavelengths around 223 nm, a shoulder of absorption was around 257 nm, and a broad hump-like shoulder was around 426 nm. These features are different from those mentioned above, which could be related to the morphology of hematite nanorods.

It is established[81] that three types of electronic transitions occur in the optical absorption spectra of Fe^{3+} substances: (a) the Fe^{3+} ligand field transition or the d−d transitions, (b) the ligand to metal charge-transfer transitions, and (c) the pair excitations resulting from the simultaneous excitations of two neighboring Fe^{3+} cations that are magnetically coupled. According to refernces 82 and 83 the absorption edge in the region from 210 to 400 nm mainly results from the ligand-to-metal charge-transfer transitions and partly from the contributions of the Fe^{3+} ligand field transition $^6A_1 \rightarrow {}^4T_1$ (^4P) at 290−310 nm, $^6A_1 \rightarrow {}^4E$ (^4D) and $^6A_1 \rightarrow {}^4T_2$ (^4D) at 360−380 nm, $^6A_1 \rightarrow {}^4E$ (^4G) at 390 nm. Absorption bands near 430 nm correspond to $^6A_1 \rightarrow {}^4E$, $^4A_1$ (^4G) ligand field transitions of Fe^{3+}. Additionally, the region from 600 to 750 nm can be assigned to the $^6A_1 \rightarrow {}^4T_2$ (^4G) ligand field transitions of Fe^{3+}. As is revealed from Figure 6, the electronic transition for the charge transfer in the wavelength region 210−400 nm dominates for the optical absorption features of the nanoparticles and nanorods, while the ligand field transitions in the range of 600−750 nm dominates for the optical absorption features of the microspheres and microcubes. The results indicated that the shape and size of the samples have great influence on their optical property.

Magnetic Properties. The magnetic hysteresis measurements of the α-Fe_2O_3 with various morphologies were carried out at 300 K in the applied magnetic field sweeping from −10 to 10 kOe. Figure 7 shows the magnetic hysteresis loops of the as-synthesized α-Fe_2O_3 samples which are indicative of the presence of ferromagnetic components. It can be seen that no saturation of the magnetization as a function of the field is observed up to the maximum applied magnetic field. The detailed values of remanent magnetization ($\mathbf{M}_r$) and coercivity (H_c) of the as-synthesized α-Fe_2O_3 samples are summarized in Table 2. It is easy to find that the remnant magnetization and coercivity force of the mesoporous hollow microspheres and microcubes are much

TABLE 2. The Values of Remanent Magnetization (M_r) and Coercivity (H_c) of the as-Synthesized Samples

samples	nanoparticles (S-1)	mesoporous hollow microspheres (S-2)	microcubes (S-4)	porous nanorods (S-5)
M_r (emu/g)	0.0087	0.1798	0.0847	0.0197
H_c (Oe)	20.31	2239	1080	65.10

larger than those of the nanoparticles. It is well-known that the magnetization of ferromagnetic materials is very sensitive to the morphologies and structures of the as-synthesized samples.[84] The assembly of the small and oriented subparticles into the superstructures (mesoporous hollow microspheres and microcubes) results in the change of the single domain to the multidomain, leading to the higher remanent magnetization and coercivity.[62] The magnetic properties of the nanorods (Figure 7d) would be very interesting because they would demonstrate the effect of shape anisotropy.[85,86] Compared with those of the nanoparticles, the higher remanent magnetization and coercivity of the nanorods may be attributed to the shape anisotropy of α-Fe_2O_3 nanorods, which prevents them from magnetizing in directions other than along their easy magnetic axes, hence leading to the higher remanent magnetization and coercivity.

CONCLUSIONS

In summary, the α-Fe_2O_3 with various morphologies has been successfully synthesized *via* an ionic liquid-assisted hydrothermal method. The hydrogen bond-*co*-$\pi-\pi$ stack mechanism is used to be responsible for the present self-assembly of the [bmim][Cl] ionic liquid in the reaction systems for the formation of the α-Fe_2O_3 with various morphologies. The dissolution-diffusion process (the effect of CH_3COOH generated from the reaction) offers the opportunity to create the porosity on the shell and is of critical importance for the formation of the hollow structures. It is believed that this process can be extended to synthesize other metal oxide with mesoporous hollow structures, and further studies are underway to broaden the applicability of this method. The UV−vis measurements suggest that the as-synthesized pure α-Fe_2O_3 with various morphologies possess different optical properties depending on the shape and size of the samples. The magnetic hysteresis measurements indicate that the as-prepared α-Fe_2O_3 samples all show ferromagnetic behavior and the superstructure and the shape anisotropy of the samples result in the interesting magnetic property evolution. The satisfactory removal capacities of the sample and the facile way of regeneration suggest that the α-Fe_2O_3 porous nanorods may be applicable in water treatment in the future. Owing to the excellent physical properties of the iron oxides, it is expected that the hematite mesoporous hollow microspheres and porous nanorods will exhibit other important applications in, for example, sensors, magnetic media, gas, and heavy metal ion adsorbents, catalytic fields, hydrogen and Li ion storage, low-dielectric-constant prosthetic materials, and support for artificial cells as well as inorganic carriers for enzyme immobilization and controlled drug delivery, *etc*. Further research is still under way.

METHODS

All the reagents were analytical grade and used without further purification. The ionic liquid 1-*n*-butyl-3-methylimidazolium chloride ([bmim][Cl]) was prepared according to the literature[87] and its general structure is shown:

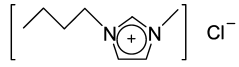

1-*n*-butyl-3-methylimidazolium chloride

One-Step Synthesis of the α-Fe_2O_3 Nanoparticles and Mesoporous Hollow Microspheres in the CH_3COOK System. In the typical synthesis procedure of hematite in the CH_3COOK system, 2 mmol of $FeCl_3 \cdot 6H_2O$ and 6 mmol of CH_3COOK were put into 20 mL of deionized water under stirring to form a homogeneous solution. Subsequently, 0, 1, 6, and 10 mmol of the [bmim][Cl] was added into the above homogeneous solution under continuous stirring, and the samples were labeled as S-0, S-1, S-2 and S-3, respectively. After stirring for 20 min, the total solution was transferred into a stainless-steel autoclave with a capacity of 30 mL, sealed and heated at 150 °C for 8 h. When the reaction was completed, the autoclave was cooled to room temperature naturally. The resultant product was collected and washed with deionized water, and anhydrous ethanol for several times until the solution was neutral. The final red product was dried in a vacuum at 80 °C for 3 h.

One-step Synthesis of the α-Fe_2O_3 Microcubes in the NaOH System. In a typical synthesis procedure of the α-Fe_2O_3 microcubes, 2 mmol of $FeCl_3 \cdot 6H_2O$ and 6 mmol of NaOH were put into 20 mL of deionized water under stirring to form a homogeneous solution. Subsequently, 6 mmol of the [bmim][Cl] was added into the above solution under continuous stirring, and the sample was labeled as S-4. The remainder of the synthesis and reaction steps are similar to those mentioned above.

Two-Step Synthesis of the α-Fe_2O_3 Porous Nanorods in the NaOH System. The first step was to prepare the α-FeOOH nanorods. Detailed synthesis procedures were the same as those for making α-Fe_2O_3 microcubes, except the amount of NaOH changed to be 20 mmol. In the second step, the α-Fe_2O_3 porous nanorods were obtained by heating the as-prepared α-FeOOH nanorods in air at 250 °C for 3 h, preserving the same rodlike morphology. The final product was labeled as S-5.

The synthetic conditions for preparing some typical samples are summarized in Table 1.

Characterization of Samples. XRD measurements were performed on a Rigaku D/max 2500 diffractometer with Cu Kα radiation (λ = 0.154056 nm) at V = 40 kV and I = 150 mA, the scanning speed was 8°/min. Morphology observations were performed on a JEOLJSM-6700F field emission scanning electron microscope (FE-SEM). TEM and HRTEM images were recorded with a Tecnai G^2 20S-Twin transmission electron microscope operating at an accelerating voltage of 120 and 200 kV, respectively. The FT-IR spectroscopy of the samples was conducted at room temperature with a KBr pellet on a VECTOR-22 (Bruker) spectrometer ranging from 400 to 4000 cm^{-1}. Ultraviolet−visible spectrum was obtained from powders suspended in deionized water using a HITACHI UV−vis recording spectrophotometer (U-3010) between 210 and 800 nm. Nitrogen adsorption−desorption isotherms were obtained on an ASAP 2020 nitrogen adsorption apparatus. The Brunauer−Emmett−Teller (BET) specific surface areas (S_{BET}) were calculated using the BET equation. Desorption isotherm was used to determine the pore size distribution using the Barret−Joyner−Halender (BJH) method. The magnetic hysteresis loops of the samples were recorded on a vibrating sample magnetometer (VSM, LDJ 9600, U.S.A.) at 300 K.

Water Treatment Experiments. For the adsorption of organic pollutant, 100 mL of methyl orange (MO) solution with a concentration of 20 mg/L was mixed with 40 mg of α-Fe_2O_3 porous nanorods (S-5). The suspension was then stirred continuously at about 25 °C. At several time intervals, small amounts of the liquid were taken to be analyzed by UV−vis absorption spectroscopy after being centrifuged for 5 min to remove the particles. The same experiment was performed on the commercial low surface area α-Fe_2O_3.

Acknowledgment. This work was supported by the National Natural of Science Foundation of China (Grant No. 20571044 and No. 20971070) and the Project Fundamental and Applied Research of Tianjin. The authors would like to thanks Prof. Yaan Cao of Nankai University for the helpful advices and discussions.

Supporting Information Available: FT-IR spectra of the as-prepared α-FeOOH nanorods and α-Fe_2O_3 porous nanorods. FT-IR spectra and frequencies of the absorption bands of the pure [bmim][Cl] and the α-Fe_2O_3/[bmim][Cl]. FE-SEM images of α-Fe_2O_3 nanoparticles, mesoporous hollow microspheres, and porous nanorods obtained in different reaction durations. This material is available free of charge *via* the Internet at http://pubs.acs.org.

REFERENCES AND NOTES

1. Cui, Y.; Lieber, C. M. Functional Nanoscale Electronic Devices Assembled Using Silicon Nanowire Building Blocks. *Science* **2001**, *291*, 851–853.
2. Hulliger, J. Chemistry and Crystal Growth. *Angew. Chem., Int. Ed.* **1994**, *33*, 143–162.
3. Caruso, F. Electrochromic Systems and the Prospects for Devices. *Adv. Mater.* **2001**, *13*, 783–793.
4. An, K.; Kwon, S. G.; Park, M.; Na, H. B.; Bail, S.; Yu, J. H.; Kim, D.; Son, J. S.; Kim, Y. W.; Song, I. C.; Moon, W. K.; Park, H. M.; Hyeon, T. W. Synthesis of Uniform Hollow Oxide Nanoparticles through Nanoscale Acid Etching. *Nano Lett.* **2008**, *8*, 4252–4258.
5. Zeng, S. Y.; Tang, K. B.; Li, T. W.; Liang, Z. H.; Wang, D.; Wang, Y. K.; Qi, Y. X.; Zhou, W. W. Facile Route for the Fabrication of Porous Hematite Nanoflowers: Its Synthesis, Growth Mechanism, Application in the Lithium Ion Battery, and Magnetic and Photocatalytic Properties. *J. Phys. Chem. C* **2008**, *112*, 4836–4843.
6. Du, D. J.; Cao, M. H. Ligand-Assisted Hydrothermal Synthesis of Hollow Fe_2O_3 Urchin-like Microstructures and Their Magnetic Properties. *J. Phys. Chem. C* **2008**, *112*, 10754–10758.
7. Wu, Z. C.; Yu, K.; Zhang, S. D.; Xie, Y. Hematite Hollow Spheres with a Mesoporous Shell: Controlled Synthesis and Applications in Gas Sensor and Lithium Ion Batteries. *J. Phys. Chem. C* **2008**, *112*, 11307–11313.
8. Yuan, R. S.; Fu, X. Z.; Wang, X. C.; Liu, P.; Wu, L.; Xu, Y. M.; Wang, X. X.; Wang, Z. Y. Template Synthesis of Hollow Metal Oxide Fibers with Hierarchical Architecture. *Chem. Mater.* **2006**, *18*, 4700–4705.
9. Bang, J. H.; Suslick, K. S. Sonochemical Synthesis of Nanosized Hollow Hematite. *J. Am. Chem. Soc.* **2007**, *129*, 2242–2243.
10. Yin, Y.; Rioux, R.; Erdonmez, C. K.; Hughes, S.; Somorjai, G. A.; Alivisatos, A. P. Formation of Hollow Nanocrystals through the Nanoscale Kirkendall Effect. *Science* **2004**, *304*, 711–714.
11. Peng, S.; Sun, S. Synthesis and Characterization of Hollow Fe_3O_4 Nanoparticles. *Angew. Chem., Int. Ed.* **2007**, *46*, 4155–4158.
12. Cabot, A.; Puntes, V. F.; Shevchenko, E.; Yin, Y.; Balcells, L.; Marcus, M. A.; Hughes, S. M.; Alivisatos, A. P. Vacancy Coalescence during Oxidation of Iron Nanoparticles. *J. Am. Chem. Soc.* **2007**, *129*, 10358–10360.
13. Fan, H. J.; Knez, M.; Scholz, R.; Nielsch, K.; Pippel, E.; Hesse, D.; Zacharias, M.; Gosele, U. Monocrystalline Spinel Nanotube Fabrication Based on the Kirkendall Effect. *Nat. Mater.* **2006**, *5*, 627–631.
14. Yu, J. G.; Guo, H. T.; Davis, S. A.; Mann, S. Fabrication of Hollow Inorganic Microspheres by Chemically Induced Self-Transformation. *Adv. Funct. Mater.* **2006**, *16*, 2035–2041.
15. Alivisatos, A. P. Semiconductor Clusters, Nanocrystals, and Quantum Dots. *Science* **1996**, *271*, 933–937.
16. Henglein, A. Small-Particle Research: Physicochemical Properties of Extremely Small Colloidal Metal and Semiconductor Particles. *Chem. Rev.* **1989**, *89*, 1861–1873.
17. Liang, X.; Wang, X.; Zhuang, J.; Chen, Y. T.; Wang, D. S.; Li, Y. D. Synthesis of Nearly Monodisperse Iron Oxide and Oxyhydroxide Nanocrystals. *Adv. Funct. Mater.* **2006**, *16*, 1805–1813.
18. Zhou, H. J.; Wang, S. S. A Facile and Mild Synthesis of 1D ZnO, CuO, and α-Fe_2O_3 Nanostructures and Nanostructured Arrays. *ACS Nano* **2008**, *2*, 944–958.
19. Woo, K.; Lee, H. J.; Ahn, J. P.; Park, Y. S. Sol−Gel Mediated Synthesis of Fe_2O_3 Nanorods. *Adv. Mater.* **2003**, *15*, 1761–1764.
20. Xiong, Y. J.; Li, Z. Q.; Li, X. X.; Hu, B.; Xie, Y. Thermally Stable Hematite Hollow Nanowires. *Inorg. Chem.* **2004**, *43*, 6540–6542.
21. Jia, C. J.; Sun, L. D.; Yan, Z. G.; You, L. P.; Luo, F.; Han, X. D.; Pang, Y. C.; Zhang, Z.; Yan, C. H. Single-Crystalline Iron Oxide Nanotubes. *Angew. Chem., Int. Ed.* **2005**, *44*, 4328–4333.
22. Zhao, Y. M.; Li, Y. H.; Ma, R. Z.; Roe, M. J.; McCartney, D. G.; Zhu, Y. Q. Growth and Characterization of Iron Oxide Nanorods/Nanobelts Prepared by a Simple Iron-Water Reaction. *Small* **2006**, *2*, 422–427.
23. Wen, X. G.; Wang, S. H.; Ding, Y.; Wang, Z. L.; Yang, S. H. Controlled Growth of Large-Area, Uniform, Vertically Aligned Arrays of α-Fe_2O_3 Nanobelts and Nanowires. *J. Phys. Chem. B* **2005**, *109*, 215–220.
24. Hu, X. L.; Yu, J. C.; Gong, J. M.; Li, Q.; Li, G. S. α-Fe_2O_3 Nanorings Prepared by a Microwave-Assisted Hydrothermal Process and Their Sensing Properties. *Adv. Mater.* **2007**, *19*, 2324–2329.
25. Jiao, F.; Harrison, A.; Jumas, J. C.; Chadwick, A. V.; Kockelmann, W.; Bruce, P. G. Ordered Mesoporous Fe_2O_3 with Crystalline Walls. *J. Am. Chem. Soc.* **2006**, *128*, 5468–5474.
26. Titirici, M. M.; Antonietti, M.; Thomas, A. A Generalized Synthesis of Metal Oxide Hollow Spheres Using a Hydrothermal Approach. *Chem. Mater.* **2006**, *18*, 3808–3812.
27. Li, L. L.; Chu, Y.; Liu, Y.; Dong, L. H. Template-Free Synthesis and Photocatalytic Properties of Novel Fe_2O_3 Hollow Spheres. *J. Phys. Chem. C* **2007**, *111*, 2123–2127.
28. Chen, D. H.; Chen, D. R.; Jiao, X. L.; Zhao, Y. T. Hollow-Structured Hematite Particles Derived from Layered Iron(Hydro)Oxyhydroxide-Surfactant Composites. *J. Mater. Chem.* **2003**, *13*, 2266–2270.
29. Gong, C. R.; Chen, D. R.; Jiao, X. L.; Wang, Q. L. Continuous Hollow α-Fe_2O_3 and α-Fe Fibers Prepared by the Sol−Gel Method. *J. Mater. Chem.* **2002**, *12*, 1844–1847.
30. Hu, X. L.; Yu, J. C. Continuous Aspect-Ratio Tuning and Fine Shape Control of Monodisperse α-Fe_2O_3 Nanocrystals by a Programmed Microwave-Hydrothermal Method. *Adv. Funct. Mater.* **2008**, *18*, 880–887.
31. Liu, L.; Kou, H. Z.; Mo, W. L.; Liu, H. J.; Wang, Y. Q. Surfactant-Assisted Synthesis of α-Fe_2O_3 Nanotubes and Nanorods with Shape-Dependent Magnetic Properties. *J. Phys. Chem. B* **2006**, *110*, 15218–15223.
32. Wu, C. Z.; Yin, P.; Zhu, X.; OuYang, C. Z.; Xie, Y. Synthesis of Hematite (α-Fe_2O_3) Nanorods: Diameter-Size and Shape Effects on Their Applications in Magnetism, Lithium Ion Battery, and Gas Sensors. *J. Phys. Chem. B* **2006**, *110*, 17806–17812.
33. Chen, J.; Xu, L. N.; Li, W. Y.; Gou, X. L. α-Fe_2O_3 Nanotubes in Gas Sensor and Lithium-Ion Battery Applications. *Adv. Mater.* **2005**, *17*, 582–587.
34. Sun, Z. Y.; Yuan, H. Q.; Liu, Z. M.; Han, B. X.; Zhang, X. R. A Highly Efficient Chemical Sensor Material for H_2S: α-Fe_2O_3

Nanotubes Fabricated by Carbon Nanotube Templates. *Adv. Mater.* **2005**, *17*, 2993–2996.
35. Jia, C. J.; Sun, L. D.; Yan, Z. G.; You, L. P.; Luo, F.; Han, X. D.; Pang, Y. C.; Zhang, Z.; Yan, C. H. Single-Crystalline Iron Oxide Nanotubes. *Angew. Chem., Int. Ed.* **2005**, *44*, 4328–4333.
36. Zhong, L. S.; Hu, J. S.; Liang, H. P.; Cao, A. M.; Song, W. G.; Wan, L. J. Self-Assembled 3D Flowerlike Iron Oxide Nanostructures and Their Application in Water Treatment. *Adv. Mater.* **2006**, *18*, 2426–2431.
37. Jain, G.; Balasubramanian, M.; Xu, J. J. Structural Studies of Lithium Intercalation in a Nanocrystalline α-Fe_2O_3 Compound. *Chem. Mater.* **2006**, *18*, 423–434.
38. Tang, B.; Wang, G. L.; Zhuo, L. H. Facile Route to α-FeOOH and α-Fe_2O_3 Nanorods and Magnetic Property of α-Fe_2O_3 Nanorods. *Inorg. Chem.* **2006**, *45*, 5196–5200.
39. Zeng, S. Y.; Tang, K. B.; Li, T. W.; Liang, Z. H.; Wang, D.; Wang, Y. K.; Zhou, W. W. Hematite Hollow Spindles and Microspheres: Selective Synthesis, Growth Mechanisms, and Application in Lithium Ion Battery and Water Treatment. *J. Phys. Chem. C* **2007**, *111*, 10217–10225.
40. Seddon, K. R. Ionic Liquids: A Taste of the Future. *Nat. Mater.* **2003**, *2*, 363–365.
41. Welton, T. Room-Temperature Ionic Liquids. Solvents for Synthesis and Catalysis. *Chem. Rev.* **1999**, *99*, 2071–2084.
42. Wasserscheid, P.; Keim, W. Ionic Liquids: New Solutions for Transition Metal Catalysis. *Angew. Chem., Int. Ed.* **2000**, *39*, 3772–3789.
43. Sheldon, R. Catalytic Reactions in Ionic Liquids. *Chem. Commun.* **2001**, *23*, 2399–2407.
44. Dzyuba, S. V.; Bartsch, R. A. Recent Advances in Applications of Room-Temperature Ionic Liquid/Supercritical CO_2 Systems. *Angew. Chem., Int. Ed.* **2003**, *42*, 148–150.
45. McEwen, A. B.; McDevitt, S. F.; Koch, V. R. Nonaqueous Electrolytes for Electrochemical Capacitors: Imidazolium Cations and Inorganic Fluorides with Organic Carbonates. *J. Electrochem. Soc.* **1997**, *144*, 84–86.
46. Dupont, J.; Suoza, R. F. D.; Suarez, P. A. Z. Ionic Liquid (Molten Salt) Phase Organometallic Catalysis. *Chem. Rev.* **2002**, *102*, 3667–3692.
47. Mele, A.; Tran, C. D.; Lacerda, S. H. D. The Structure of a Room-Temperature Ionic Liquid with and without Trace Amounts of Water: The Role of C−H···O and C−H···F Interactions in 1-*n*-Butyl-3-methylimidazolium Tetrafluoroborate. *Angew. Chem., Int. Ed.* **2003**, *42*, 4364–4366.
48. Endres, F.; Bukowski, M.; Hempelmann, R.; Natter, H. Electrodeposition of Nanocrystalline Metals and Alloys from Ionic Liquids. *Angew. Chem., Int. Ed.* **2003**, *42*, 3428–3430.
49. Liu, D. P.; Li, G. D.; Su, Y.; Chen, J. S. Highly Luminescent ZnO Nanocrystals Stabilized by Ionic-Liquid Components. *Angew. Chem., Int. Ed.* **2006**, *45*, 7370–7373.
50. Cooper, E. R.; Andrews, C. D.; Wheatley, P. S.; Webb, P. B.; Wormald, P.; Morris, R. E. Ionic Liquids and Eutectic Mixtures as Solvent and Template in Synthesis of Zeolite Analogues. *Nature* **2004**, *430*, 1012–1016.
51. Trewyn, B. G.; Whitman, C. M.; Lin, V. S. Y. Morphological Control of Room-Temperature Ionic Liquid Templated Mesoporous Silica Nanoparticles for Controlled Release of Antibacterial Agents. *Nano Lett.* **2004**, *4*, 2139–2143.
52. Cao, S. W.; Zhu, Y. J. Iron Oxide Hollow Spheres: Microwave-Hydrothermal Ionic Liquid Preparation, Formation Mechanism, Crystal Phase and Morphology Control and Properties. *Acta Mater.* **2009**, *57*, 2154–2165.
53. Zheng, W. J.; Liu, X. D.; Yan, Z. Y.; Zhu, L. J. Ionic Liquid-Assisted Synthesis of Large-Scale TiO_2 Nanoparticles with Controllable Phase by Hydrolysis of $TiCl_4$. *ACS Nano* **2009**, *3* (1), 115–122.
54. Wang, L.; Chang, L. X.; Zhao, B.; Yuan, Z. Y.; Shao, G. S.; Zheng, W. J. Systematic Investigation on Morphologies, Forming Mechanism, Photocatalytic, and Photoluminescent Properties of ZnO Nanostructures Constructed in Ionic Liquids. *Inorg. Chem.* **2008**, *47*, 1443–1452.
55. Ruan, H. D.; Frost, R. L.; Kloprogge, J. T.; Duong, L. Infrared Spectroscopy of Goethite Dehydroxylation: III. FT-IR Microscopy of in situ Study of the Thermal Transformation of Goethite to Hematite. *Spectrochim. Acta A.* **2002**, *58*, 967–981.
56. Jone, F.; Farrow, J. B.; Bronswijk, W. An Infare Study of a Polyacrylate Flocculant Adsorbed on Hematite. *Langmuir* **1998**, *14*, 6512–6517.
57. Liu, X. D.; Ma, J. M.; Peng, P.; Zheng, W. J. Ionic Liquid-Assisted Complex-Solvothermal Synthesis of ZnSe Hollow Microspheres. *Mater. Sci. Eng., B* **2008**, *150*, 89–94.
58. Antonietti, M.; Kuang, D.; Smarsly, B.; Zhou, Y. Ionic Liquids for the Convenient Synthesis of Functional Nanoparticles and Other Inorganic Nanostructures. *Angew. Chem., Int. Ed.* **2004**, *43*, 4988–4992.
59. Li, J.; Zeng, H. C. Hollowing Sn-Doped TiO_2 Nanospheres *via* Ostwald Ripening. *J. Am. Chem. Soc.* **2007**, *129*, 15839–15847.
60. Penn, R. L.; Banfield, J. F. Imperfect Oriented Attachment: Dislocation Generation in Defect-Free Nanocrystals. *Science* **1998**, *281*, 969–971.
61. Zhang, Z.; Sun, H.; Shao, X.; Li, D.; Yu, H.; Han, M. Three-Dimensionally Oriented Aggregation of a Few Hundred Nanoparticles into Monocrystalline Architectures. *Adv. Mater.* **2005**, *17*, 42–47.
62. Zhu, L. P.; Xiao, H. M.; Fu, S. Y. Template-Free Synthesis of Monodispersed and Single-Crystalline Cantaloupe-like Fe_2O_3 Superstructures. *Cryst. Growth Des.* **2007**, *7*, 177–182.
63. Lian, J. B.; Kim, T.; Liu, X. D.; Ma, J. M.; Zheng, W. J. Ionothermal Synthesis of Turbostratic Boron Nitride Nanoflakes at Low Temperature. *J. Phys. Chem. C* **2009**, *113*, 9135–9140.
64. Zhou, Y.; Schattka, J. H.; Antonietti, M. Room-Temperature Ionic Liquids as Template to Monolithic Mesoporous Silica with Wormlike Pores *via* a Sol−Gel Nanocasting Technique. *Nano Lett.* **2004**, *4*, 477–481.
65. Zhou, Y.; Antonietti, M. Synthesis of Very Small TiO_2 Nanocrystals in a Room-Temperature Ionic Liquid and Their Self-Assembly toward Mesoporous Spherical Aggregates. *J. Am. Chem. Soc.* **2003**, *125*, 14960–14961.
66. Taubert, A. CuCl Nanoplatelets from an Ionic Liquid Crystal Precursor. *Angew. Chem., Int. Ed.* **2004**, *43*, 5380–5382.
67. Nakashima, T.; Kimizuka, N. Interfacial Synthesis of Hollow TiO_2 Microspheres in Ionic Liquids. *J. Am. Chem. Soc.* **2003**, *125*, 6386–6387.
68. Kaper, H.; Endres, F.; Djerdj, I.; Antonietti, M.; Smarsly, B. M.; Maier, J.; Hu, Y. S. Direct Low-Temperature Synthesis of Rutite Nanostructures in Ionic Liquids. *Small* **2007**, *10*, 1753–1763.
69. Wu, L. Y.; Lian, J. B.; Sun, G. X.; Kong, X. R.; Zheng, W. J. Synthesis of Zinc Hydroxyfluoride Nanofibers through an Ionic Liquid Assisted Microwave Irradiation Method. *Eur. J. Inorg. Chem.* **2009**, *20*, 2897–2900.
70. Lu, J.; Jiao, X. L.; Chen, D. R.; Li, W. Solvothermal Synthesis and Characterization of Fe_3O_4 and γ-Fe_2O_3 Nanoplates. *J. Phys. Chem. C* **2009**, *113*, 4012–4017.
71. Comminges, C.; Barhdadi, R.; Laurent, M.; Troupel, M. Determination of Viscosity, Ionic Conductivity, and Diffusion Coefficients in Some Binary Systems: Ionic Liquids + Molecular Solvents. *J. Chem. Eng. Data* **2006**, *51*, 680–685.
72. Wang, J. J.; Tian, Y.; Zhao, Y.; Zhuo, K. L. A Volumetric and Viscosity Study for the Mixtures of 1-*n*-Butyl-3-methylimidazolium Tetrafluoroborate Ionic Liquid with Acetonitrile, Dichloromethane, 2-Butanone and *N*,*N*-Dimethylformamide. *Green Chem.* **2003**, *5*, 618–622.
73. Naono, H.; Nakai, K.; Sueyoshi, T.; Yagi, H. Porous Texture in Hematite Derived from Goethite: Mechanism of Thermal Decomposition of Goethite. *J. Colloid Interface Sci.* **1987**, *120*, 439–450.
74. Jaricot, S. C.; Brioude, A.; Miele, P. Ultrathin Polycrystalline Hematite and Goethite-Hematite Core−Shell Nanorods. *Langmuir* **2009**, *25*, 2551–2553.

75. Cudennec, Y.; Lecerf, A. The Transformation of Ferrihydrite into Goethite or Hematite, Revisited. *J. Solid State Chem.* **2006**, *179*, 716–722.
76. Cao, S. W.; Zhu, Y. J. Hierarchically Nanostructured α-Fe_2O_3 Hollow Spheres: Preparation, Growth Mechanism, Photocatalytic Property, and Application in Water Treatment. *J. Phys. Chem. C* **2008**, *112*, 6253–6257.
77. Yu, C. H.; Dong, X. P.; Guo, L. M.; Li, J. T.; Qin, F.; Zhang, L. X.; Shi, J. L.; Yan, D. S. Template-Free Preparation of Mesoporous Fe_2O_3 and Its Application as Absorbents. *J. Phys. Chem. C* **2008**, *112*, 13378–13382.
78. Zhou, H. S.; Mito, A.; Kundu, D.; Honma, I. Nonlinear Optical Susceptibility of Fe_2O_3 Thin Film Synthesized by a Modified Sol−Gel Method. *J. Sol−Gel Sci. Technol.* **2000**, *19*, 539–541.
79. Wang, S. B.; Min, Y. L.; Yu, S. H. Synthesis and Magnetic Properties of Uniform Hematite Nanocubes. *J. Phys. Chem. C* **2007**, *111*, 3551–3554.
80. Zhang, J. T.; Liu, J. F.; Peng, Q.; Wang, X.; Li, Y. D. Nearly Monodisperse Cu_2O and CuO Nanospheres: Preparation and Applications for Sensitive Gas Sensors. *Chem. Mater.* **2006**, *18*, 867–871.
81. He, Y. P.; Miao, Y. M.; Li, C. R.; Wang, S. Q.; Cao, L.; Xie, S. S.; Yang, G. Z.; Zou, B. S.; Burda, C. Size and Structure Effect on Optical Transitions of Iron Oxide Nanocrystals. *Phys. Rev. B* **2005**, *71*, 125411–125420.
82. Sherman, D. M.; Waite, T. D. Electronic Spectra of Fe^{3+} Oxides and Oxide Hydroxides in the Near-IR to Near-UV. *Am. Mineral.* **1985**, *70*, 1262–1269.
83. Hashimoto, T.; Yamada, T.; Yoko, T. Third-Order Nonlinear Optical Properties of Sol−Gel Derived α-Fe_2O_3, γ-Fe_2O_3, and Fe_3O_4 Thin Films. *J. Appl. Phys.* **1996**, *80*, 3184–3190.
84. Sorescu, M.; Brand, R. A.; Tarabasanu, D. M.; Diamandescu, L. The Crucial Role of Particle Morphology in the Magnetic Properties of Hematite. *J. Appl. Phys.* **1999**, *85*, 5546–5548.
85. Park, S. J.; Kim, S.; Lee, S.; Khim, Z.; Char, K.; Hyeon, T. Synthesis and Magnetic Studies of Uniform Iron Nanorods and Nanospheres. *J. Am. Chem. Soc.* **2000**, *122*, 8581–8582.
86. Wang, J.; Chen, Q. W.; Zeng, C.; Hou, B. Y. Magnetic-Field-Induced Growth of Single-Crystalline Fe_3O_4 Nanowires. *Adv. Mater.* **2004**, *16*, 137–140.
87. Hasan, M.; Kozhevnikov, I. V.; Siddiqui, M. R. H.; Steiner, A.; Winterton, N. Gold Compounds as Ionic Liquids: Synthesis, Structures, and Thermal Properties of *N,N*-Dialkylimidazolium Tetrachloroaurate Salts. *Inorg. Chem.* **1999**, *38*, 5637–5641.